A&A 427, 397–413 (2004)
DOI: 10.1051/0004-6361:20041304

Astronomy & Astrophysics

Spectroscopy of clusters in the ESO Distant Cluster Survey (EDisCS)⋆,⋆⋆

Redshifts, velocity dispersions and substructure for 5 clusters

C. Halliday[1,5], B. Milvang-Jensen[2], S. Poirier[3], B. M. Poggianti[1], P. Jablonka[3], A. Aragón-Salamanca[4], R. P. Saglia[2], G. De Lucia[5], R. Pelló[6], L. Simard[7], D. I. Clowe[8,9], G. Rudnick[5], J. J. Dalcanton[10], S. D. M. White[5], and D. Zaritsky[9]

[1] Osservatorio Astronomico, vicolo dell'Osservatorio 5, 35122 Padova, Italy
e-mail: [halliday;poggianti]@pd.astro.it
[2] Max-Planck Institut für extraterrestrische Physik, Giessenbachstrasse, 85748 Garching, Germany
e-mail: [milvang;saglia]@mpe.mpg.de
[3] GEPI, CNRS-UMR8111, Observatoire de Paris, section de Meudon, 5 Place Jules Janssen, 92195 Meudon Cedex, France
e-mail: Pascale.Jablonka@obspm.fr
[4] School of Physics and Astronomy, University of Nottingham, University Park, NG7 2RD, UK
e-mail: Alfonso.Aragon@nottingham.ac.uk
[5] Max-Planck-Institut für Astrophysik, Karl-Schwarschild-Str. 1, Postfach 1317, 85741 Garching, Germany
e-mail: [halliday;lucia;grudnick;swhite]@mpa-garching.mpg.de
[6] Laboratoire d'Astrophysique, UMR 5572, Observatoire Midi-Pyrenees, 14 Avenue E. Belin, 31400 Toulouse, France
e-mail: Roser.Pello@ast.obs-mip.fr
[7] Herzberg Institute of Astrophysics, National Research Council of Canada, Victoria, BC V9E 2E7, Canada
e-mail: Luc.Simard@nrc.ca
[8] Institut für Astrophysik und Extraterrestrische Forschung, Universität Bonn, Auf dem Hugel 71, 53121 Bonn, Germany
[9] Steward Observatory, University of Arizona, 933 North Cherry Avenue, Tucson, AZ 85721, USA
e-mail: [clowe;dzaritsky]@as.arizona.edu
[10] Astronomy Department, University of Washington, Box 351580, Seattle, WA 98195, USA
e-mail: jd@astro.washington.edu

Received 17 May 2004 / Accepted 28 July 2004

Abstract. We present spectroscopic observations of galaxies in 4 clusters at $z = 0.7-0.8$ and in one cluster at $z \sim 0.5$ obtained with the FORS2 spectrograph on the VLT as part of the ESO Distant Cluster Survey (EDisCS), a photometric and spectroscopic survey of 20 intermediate to high redshift clusters. We describe our target selection, mask design, observation and data reduction procedures, using these first 5 clusters to demonstrate how our strategies maximise the number of cluster members for which we obtain spectroscopy. We present catalogues containing positions, I-band magnitudes and spectroscopic redshifts for galaxies in the fields of our 5 clusters. These contain 236 cluster members, with the number of members per cluster ranging from 30 to 67. Our spectroscopic success rate, i.e. the fraction of spectroscopic targets which are cluster members, averages 50% and ranges from 30% to 75%. We use a robust biweight estimator to measure cluster velocity dispersions from our spectroscopic redshift samples. We also make a first assessment of substructure within our clusters. The velocity dispersions range from 400 to 1100 km s^{-1}. Some of the redshift distributions are significantly non-Gaussian and we find evidence for significant substructure in two clusters, one at $z \sim 0.79$ and the other at $z \sim 0.54$. Both have velocity dispersions exceeding 1000 km s^{-1} but are clearly not fully virialised; their velocity dispersions may thus be a poor indicator of their masses. The properties of these first 5 EDisCS clusters span a wide range in redshift, velocity dispersion, richness and substructure, but are representative of the sample as a whole. Spectroscopy for the full dataset will allow a comprehensive study of galaxy evolution as a function of cluster environment and redshift.

Key words. galaxies: clusters: general – galaxies: distances and redshifts – galaxies: evolution

⋆ Based on observations obtained at the ESO Very Large Telescope (VLT) as part of the Large Programme 166.A–0162 (the ESO Distant Cluster Survey).

⋆⋆ Full Table 4 is only available in electronic form at the CDS via anoymous ftp to cdsarc.u-strasbg.fr (130.79.125.5) or via http://cdsweb.u-strasbg.fr/cgi-bin/qcat?J/A+A/427/397

1. Introduction

Galaxy clusters are convenient and popular sites for studying environmental influences on galaxy evolution and the systematic analysis of large cluster samples is an important step towards a quantitative understanding of the processes involved. Large area cluster searches began with the pioneering photographic surveys of Abell (1958), Zwicky et al. (1968) and Shectman (1985). More recently, surveys for high-redshift clusters (e.g. Gunn et al. 1986; Gioia et al. 1990; Couch et al. 1991; Postman et al. 1996; Gladders & Yee 2000; Gonzalez et al. 2001) have begun to provide large enough samples to allow an exploration of the evolution of clusters and the galaxies within them out to significant lookback times.

Spectroscopic surveys of the full galaxy population of distant galaxy clusters are few in number. At intermediate redshift they include the studies of Couch & Sharples (1987), and of the CNOC and MORPHs collaborations (Yee et al. 1996; Balogh et al. 1997; Dressler et al. 1999; Poggianti et al. 1999), as well as the studies of individual clusters by van Dokkum, Kelson, Tran and collaborators (e.g. Kelson et al. 1997; Tran et al. 2003). At higher redshift there is the survey by Postman and collaborators (Postman et al. 1998; Postman et al. 2001) and the study of the single very rich cluster MS1054-03 by van Dokkum et al. (2000). Such surveys have contributed substantially to our understanding of the star formation histories of cluster galaxies, revealing strong evolution in their average star formation activity since $z \sim 0.5$, thus over the last 5 Gyr. At redshifts beyond 0.5, too few clusters have been studied so far to draw strong conclusions about galaxy evolution and the dependence of galaxy properties on environment (e.g. van Dokkum et al. 2000; Postman et al. 1998; Postman et al. 2001).

Measurements of cluster velocity dispersions are often used to estimate cluster masses (e.g. Fisher et al. 1998; Tran et al. 1999; Borgani et al. 1999; Lubin et al. 2002). Early measurements of velocity dispersions (e.g. Danese et al. 1980) usually assumed a Gaussian velocity distribution. As datasets have increased in quality and size, significant deviations from Gaussian behaviour have often been found (e.g. Zabludoff et al. 1993; Fisher et al. 1998). These are likely associated with the substantial structural irregularities (usually termed substructure) which are observed in many clusters (Geller & Beers 1982; Dressler & Shectman 1988). Any statistic used to estimate cluster velocity dispersion should therefore be robust against outliers and against variations in the shape of the underlying velocity distribution (Beers et al. 1990). Cluster velocity dispersion measurements have been published for only a small number of high redshift clusters (e.g. Tran et al. 1999; Lubin et al. 2002) and analyses of cluster substructure at such high redshift are scarce. In this paper we present velocity dispersions and substructure analyses for 5 of the high redshift clusters in the ESO Distant Cluster Survey (EDisCS).

The ESO Distant Cluster Survey is a photometric and spectroscopic survey of 20 clusters selected from the Las Campanas Distant Cluster Survey (LCDCS) (Gonzalez et al. 2001). Clusters in the LCDCS were selected to be amongst the most significant surface brightness peaks in a smoothed drift scan map of 110 square degrees of the southern sky. One half of our sample was chosen to have high estimated redshift in the LCDCS ($z_{\rm est} \sim 0.8$) while the other half was chosen to have intermediate estimated redshift ($z_{\rm est} \sim 0.5$). The apparent reality of these candidates was established before inclusion in the final EDisCS sample by moderate depth VLT imaging in two passbands. This allowed verification of the expected overabundance, colour and magnitude of red sequence galaxies (Gonzalez et al. 2002).

Our EDisCS observing programme is now complete. It involves deep optical photometry using FORS2 at the VLT (14 nights), near-IR photometry with the SOFI instrument at the NTT (20 nights), and multi-slit spectroscopy using the FORS2 spectrograph at the VLT (22 nights). Our optical photometry comprises V, R and I imaging for the 10 high-redshift clusters and B, $V$and I imaging for the 10 intermediate-redshift clusters (White et al. 2004, in preparation). The field of view of the FORS2 instrument is $6.8' \times 6.8'$. After dithering, the field of view with the maximum depth of exposure in our imaging data was approximately $6.5' \times 6.5'$. Near-IR data in J and K will be presented in Aragón-Salamanca et al. 2004 (in preparation). The field of view of our SOFI images, taking account of the dithering and overlapping of exposures, was $6.0' \times 4.2'$ for our clusters at $z \sim 0.5$ and $5.4' \times 4.2'$ for our clusters at $z \sim 0.8$: see Aragón-Salamanca et al. (2004, in preparation, for details). This ground-based dataset has been complemented in February–June 2003 by 80 orbits of HST ACS imaging for our 10 high-redshift clusters (Desai et al. 2004, in preparation).

The EDisCS project aims to investigate galaxy morphology, structure, masses, stellar populations and star formation histories as a function of both redshift and cluster environment, and to study cluster mass and structure. Our spectroscopy allows cluster membership to be defined using precise redshifts and it constrains the evolutionary histories of galaxies in dense environments by providing estimates of (or at least constraints on) star formation rates and histories, chemical abundances, internal kinematics, and stellar and dynamical masses. We are studying both early- and late-type galaxy evolution by measurement of the Fundamental Plane and Tully-Fisher scaling relations as a function of redshift and environment. The ages and metallicities of cluster absorption-line galaxies are being constrained using absorption line-strength index measurements and evolutionary population synthesis models. The star formation histories of cluster galaxies are being studied using absorption line and emission line information, as well as broad-band spectral energy distributions and HST/ACS morphologies.

In this paper we present the procedures we have adopted to carry out the spectroscopic part of the EDisCS programme, and we give first results for a set of five clusters. The main focus of this paper is a presentation of the spectroscopic data for these clusters, one of which is at $z \sim 0.5$ (Cl 1232.5−1250) while the other four are at $z = 0.7$–0.8 (Cl 1040.7−1155, Cl 1054.4−1146, Cl 1054.7−1245 and Cl 1216.8−1201). We will abbreviate these names as Cl 1232, Cl 1040, Cl 1054−11, Cl 1054−12 and Cl 1216, respectively, in the following. In Sect. 2 we describe our target selection strategy, our mask design and our VLT FORS2 observations. In Sect. 3 we describe the reduction of these VLT FORS2 observations. In Sect. 4 we present galaxy redshift measurements and spectroscopic

Table 1. The EDisCS spectroscopic observing runs.

Run	Dates (noon-to-noon)	Number of nights Total	Usable
Run 1	06 Feb. 2002–09 Feb. 2002	3	1.6
Run 2	11 Mar. 2002–19 Mar. 2002	8	6.9
Run 3	26 Mar. 2003–06 Apr. 2003	11	11.0
Run 4	23 Mar. 2004–26 Mar. 2004	3	3.0

catalogues, and we assess our observational completeness and the success of our observing strategy. In Sect. 5 we present velocity dispersion estimates for our clusters. In Sect. 6 we study cluster substructure using maps of galaxy positions and also the Dressler-Shectman (1988) method. A summary is provided in Sect. 7.

2. Observations

Spectroscopic observations were completed during the four observing runs listed in Table 1. During our first run we took relatively short exposures to establish the reality of our clusters, to measure their redshifts and to tune our photometric redshifts to allow stricter selection criteria for subsequent runs. During our second run deep spectroscopic exposures were completed for the 5 EDisCS clusters discussed in this paper, 4 high redshift clusters and 1 intermediate redshift cluster. Short exposures were acquired in addition in this second run for EDisCS clusters for which data were not obtained in the first run due to bad weather. During the third run, one or two additional masks were observed for the 5 clusters presented in this paper, and long-exposure data were obtained for most of the other EDisCS clusters. Finally, in the fourth run we completed our spectroscopic programme for the full sample, obtaining data for clusters not discussed in this paper.

In Sect. 2.1 we describe the target selection strategy. In Sect. 2.2 we describe the VLT FORS2 MXU mask preparation. In Sect. 2.3 we describe the observations themselves.

2.1. Target selection strategy

When selecting the spectroscopic targets, the main aim was to produce a well-defined sample of cluster galaxies that was as statistically complete as possible. Given the available imaging data, selection in the I-band was the obvious choice: such red-band selection reduces biases towards star-forming or unextincted galaxies. Our parent sample consisted of all objects with $18.6 \leq I \leq 22$ for the $z \sim 0.5$ cluster candidates and $19.5 \leq I \leq 23$ for the $z \sim 0.8$ ones. Since we are completing spectroscopy using $1''$ slits, for our target selection we used $1''$ radius aperture magnitudes. The bright magnitude cut was imposed to reject galaxies that are too bright to be cluster members at the expected redshifts of our clusters. These bright magnitude limits are $\sim$1 mag brighter than brightest cluster galaxies at $z \sim 0.5$ and $z \sim 0.8$ respectively (Aragón-Salamanca et al. 1998), and are thus very conservative.

Such straightforward I-band selection produces a sample where the selection criteria are easy to model and to reproduce, but where the contamination by non-cluster galaxies and by stars is quite high. For example, for the extremely rich $z = 0.83$ cluster MS 1054-03, Keck spectroscopy for an I-band selected sample found that only $\simeq$40% of the galaxies with measured redshifts were actually cluster members (van Dokkum et al. 2000). Our optically-selected clusters have a range of richnesses, so we would expect our success rate for a purely I-band selected sample to be substantially worse than this in most cases. To avoid wasting telescope time, we decided to use the available imaging information to impose additional selection criteria. The aim is to reject a significant fraction of non-members while keeping the sample of cluster galaxies as close as possible to an I-band selected one. Since completeness of our cluster samples is our main concern, our rejection criteria were chosen to be conservative.

Our target rejection criteria were based primarily on photometric redshifts obtained with a modified version of the code `hyperz`[1] (Bolzonella et al. 2000). Photometric redshifts have proven to be quite reliable when a reasonably-complete set of photometry, including near-infrared bands, is available. When tested against spectroscopic redshifts, the typical errors in the photometric redshifts are $\simeq$0.1 (Bolzonella et al. 2000; Pelló et al. 2004, in preparation). The `hyperz` code is based on a standard SED fitting minimization procedure, broad-band filters allowing the detection of strong spectral features, such as the 4000 Å break, the Lyman break or strong emission lines. The template library used includes 6 evolutionary synthetic SEDs computed using the Bruzual & Charlot code (Bruzual & Charlot 1993), matching the observed colours of local field galaxies at $z \sim 0$, from E to Im type, in addition to a set of empirical SEDs compiled by Coleman et al. (1980), and 2 starburst galaxies from the Kinney et al. (1996) template library (SB1 and SB2). The internal reddening law is taken from Calzetti et al. (2000), and considered as a free parameter with A_V ranging between 0 and 1.5 mag ($E(B-V)$ between 0 and $\sim$0.37 mag). For each cluster field a correction for galactic extinction was included using the value of $E(B-V)$ derived from Schlegel et al. (1998) for the cluster centre. Galactic $E(B-V)$ corrections in the EDisCS fields typically range between 0.03 and 0.08 mag. The reader is referred to the reference paper (Pelló et al. 2004, in preparation) for a more detailed description.

Photometric redshift accuracy depends on the wavelength domain covered by the photometric SEDs, i.e. the filter set. The set of filters used by EDisCS was designed to cover the relevant wavelength domain in the restframe of mid $z \sim 0.5$ and high $z \sim 0.8$ clusters, in particular to bracket the 4000 Å break within the relevant redshift intervals. As explained in White et al. (2004), deep optical photometry was obtained using FORS2 at the VLT, in *BVI* and *VRI* bands respectively for our mid-z and the high-z clusters. In addition, deep near-IR images were obtained with SOFI at NTT, in K' and JK' bands respectively for our mid-z and the high-z clusters (see Aragón-Salamanca et al. 2004, in preparation for details). These optical and near-IR band data were used to derive our photometric redshifts.

[1] `http://webast.obs-mip.fr/hyperz/`

After imposing the magnitude cuts described above, targets were selected if their photometric redshift obeyed $z_{\rm clus} - 0.2 \leq z_{\rm phot} \leq z_{\rm clus} + 0.2$, where $z_{\rm clus}$ was the estimated cluster redshift. The cluster redshift was estimated, initially, from the peak in the photometric redshift histograms (see Pelló et al. 2004, in preparation). After our first short-exposure masks were observed and analysed, cluster redshifts based on our spectroscopy were used instead.

As an additional measure to ensure that no likely cluster members were dropped from the sample, we took into account that the photometric redshift code provides not only a "best guess" photometric redshift, but also a redshift probability distribution for each object. Objects with $z_{\rm phot}$ outside the $z_{\rm clus} \pm 0.2$ interval were selected for spectroscopy if the χ^2-based probability of the best fit provided by the photometric redshift code at the cluster redshift was larger than 50%. Because the redshift probability distributions were reasonably peaked for most objects, this only increased the number of selected targets by 2–3%. For this reason, the exact value of the probability threshold for selection had very little effect on our target list (see Pelló et al. 2004, in preparation for details).

Finally, the photometric redshift code also provides some information to help with star-galaxy separation. For each object, the code computes two independent values, $N_{\rm G}$ and N_*, based on how well the photometry corresponds to a galactic or a stellar SED (Pelló et al. 2004, in preparation). $N_{\rm G} = 0$ means "the object is almost certainly not a galaxy"; $N_{\rm G} = 1$ "the object could be a galaxy"; and $N_{\rm G} = 2$ "the object is almost certainly a galaxy". Similarly, N_* can have values 0, 1 and 2 with similar meanings but for stars. Objects with $N_{\rm G} = 0$ and $N_* \geq 1$ were excluded from the spectroscopic sample as very probable stars. As a safety precaution, we have checked that the vast majority (at least ≃95%) of the objects rejected as probable stars based on their photometry have stellar PSFs, while virtually all the rest are blended objects. Moreover, each spectroscopic mask had slits placed on several stars (typically 3–5) for acquisition purposes. These stars were selected from the objects photometrically classified as very probable stars. There were 52 such objects in the masks of the five clusters discussed in this paper, and the spectroscopy confirmed all of them as stars.

Indeed, the photometric criteria used to remove stars from the target list is more conservative than using the PSF alone: a significant number of objects with stellar PSFs remained in the target list in the 2002 observing runs, and they were confirmed as stars by the spectroscopy. To further reduce our stellar contamination, in the 2003 and 2004 observing runs we decided to reject in addition objects which have clear stellar PSFs in the I-band images. This decision was based on the excellent image quality of our I-band data (median seeing 0.6″, cf. White et al. 2004), and on the experience gained in the 2002 runs. For each cluster, a set of 20–30 bona-fide stars was selected, their ellipticities and $FWHM$s measured, and the mean ($\langle FWHM \rangle$) and standard deviation of the $FWHM$s (σ_{FWHM}) determined. Then, objects were removed from the target list of that cluster if their $FWHM$ was less than $\langle FWHM \rangle + 2\sigma_{FWHM}$ and their ellipticities were less than 0.1. Typically, $\langle FWHM \rangle \simeq 0.6''$ and $\sigma_{FWHM} \simeq 0.05''$. This procedure removed only ∼5% of the candidate targets. Note that the results presented in this paper are based mostly on spectroscopy obtained in 2002, and thus this additional selection criterion was not applied there. Had we applied it, out of the 231 spectroscopically-confirmed cluster members, not a single one would have been rejected on the basis of its PSF. Indeed, not a single object with spectroscopically-confirmed redshift larger than ≃ 0.0 would have been rejected on the basis of its PSF.

In addition to these photometric criteria, the mask design imposes geometric constraints in order to avoid overlapping spectra and to ensure the necessary wavelength coverage (see next section). In the mask design process, it was sometimes impossible to find targets that fulfilled all the selection criteria at a given mask location. In such cases, in order to fill the masks, slits were placed on an ad hoc basis on objects that had not been selected as cluster galaxy candidates, and therefore were expected to be field galaxies based on their photometric redshifts. A test of how well our selection worked is provided by the number of such photometrically-selected field galaxies that turned out to be cluster members. For the five clusters discussed in this paper, redshifts were obtained for 65 such galaxies, and none of them turned out to be a cluster member. Thus we are reasonably confident that our selection criteria have excluded, at most, 1–2% of real cluster galaxies above our I-band limit. Once the spectroscopy for our complete EDisCS data set is analysed, we will have tighter constraints on this number.

A measure of the effectiveness of our selection procedure is that our success rate, measured as the fraction of spectroscopic targets that turned out to be cluster members, is, on average, ≃50% for the five clusters described in this paper. If we had used a pure I-band selection, the success rate would have been under 30%, and our use of 8-m telescope time substantially less efficient. In summary, we are quite confident that our target selection process yielded a cluster galaxy sample that is very close to a purely I-band selected one, but with almost twice as many spectroscopically-confirmed cluster members as would have been the case if we had not made use of photo-z rejection of non-members.

2.2. Automatic creation of the masks

We developed a program to automatically place MXU mask slits on targeted galaxies (Poirier 2004).

Mask design was performed using our EDisCS I-band images, since these best correspond to the wavelength domain of the grism 600RI+19 which we had chosen for our spectroscopy. We fixed the right ascension axis to be parallel to the X axis of the detectors. The centre of the mask was chosen in order to maximize the number of galaxies to be observed. For the 2002 observations we matched the spectroscopic field centre with the position of the brightest cluster galaxy (BCG) in X and the center of the photometric image in Y. For 2003, we had to take into account the change of FORS2 CCDs and in particular a 5.″5 gap between the two new detectors. We allowed a 10″ to 20″ shift along the Y axis.

Reference stars were selected to aid the calculation of shifts in RA, Dec and rotation required to precisely align each MXU mask on the sky. Seven reference stars were chosen for each mask to have 17.5 mag $< I <$ 19.9 mag and to be uniformly distributed across the field of view. Short (5″) slits were placed

on 2–3 stars to help optimise the final mask alignment and to allow seeing to be measured during observations.

Our science aims required the observation of a minimum spectral region including the [OII]λ3727 and H$\delta\lambda$4101 spectral lines for the cluster galaxy candidates. This restframe domain was shifted for each cluster, according to its photometric redshift for the preparation of our first February 2002 spectroscopic run, or using the spectroscopic cluster redshift for the preparation of our long-exposure masks.

The slit width was 1″. We selected slit lengths of 10″ for cluster galaxy candidates, 6″ for field galaxy candidates, and 5″ for star reference slits. For the cluster BCG galaxy a 10″ slit was not sufficiently long and we chose a slit length equal to $10 \times FWHM$. We fixed a minimum separation between slits of 1″ to avoid any superposition of spectra. The galaxies were centered in the slits when possible, otherwise at least 3″ away from the slit edges to ensure good sky substraction.

In 2002, slits on cluster galaxy candidates were aligned with the galaxy major axis when `hyperz` indicated a spiral type spectral energy distribution. The position angle provided by SExtractor was used as long as it did not exceed 45 degrees. A vertical slit was selected for all remaining galaxies. After reduction of the 2002 runs, we identified a number of emission line galaxies which had been classified as ellipticals by `hyperz`. In subsequent runs slits were aligned with the major axis for all galaxies provided that the slit inclination angle did not exceed 45 degrees.

Galaxies were selected by order of priority: 1) BCG or the closest possible galaxy; 2) confirmed cluster galaxy, or target for which the redshift determination was still ambiguous in the short exposure spectra; 3) cluster galaxy candidates, based on the criteria presented in Sect. 2.1; 4) star slits; 5) field galaxy candidates. For each of the categories 1 to 3, the spectroscopic target selection was completed so that the brightest cluster member candidates in the considered region of the mask were selected first.

Once all possible primary targets had been exhausted, we filled masks with 6″ slits placed preferentially on cluster galaxy candidates, with no constraint on the wavelength range. Finally a visual inspection of all masks was performed.

2.3. Observations

Spectroscopic data were acquired during four observing runs using the MXU multi-object mask facility of the FORS2 spectrograph mounted on the VLT Yepun UT4 telescope, ESO Paranal, as described in Tables 1 and 3. Details of our observational setup are provided in Table 2.

The observing log is given in Table 3. For each of the 20 EDisCS clusters the total exposure time for each mask observed in the four observing runs is listed. The individual exposures were typically 1800 s. The masks are labelled in a simple way: masks used in run 1 are called mask 1, masks used in run 2 are called mask 2, 3 and 4, masks used in run 3 are called mask 5, 6, 7 and 8, and masks used in run 4 are called mask 9, 10 and 11. Since not all clusters were observed in run 1, not all clusters have a "mask 1", et cetera.

Table 2. The MXU multi-slit instrumental set-up.

Run	Run 1 + 2	Run 3 + 4
Telescope	VLT–UT4	
Instrument	FORS2	
Mode	MXU (i.e. mask multi-slit)	
Grism	GRIS_600RI+19	
Filter	GG435	
Spectral resolution	6.6 Å *FWHM*	
Detector(s)	Site	$2 \times$ MIT
Detector size	2048×2048	$2 \times (2048 \times 1024)^a$
Pixel size	24 μm $\times$ 24 μm	30 μm $\times$ 30 μm^a
Readout noise	5.41 e$^-$	3.15 e$^-$
Conversion factor	1.91 e$^-$/ADU	0.70 e$^-$/ADU
MXU slit width	1.″0	1.″0
Spatial scale	0.″20/pixel	0.″25/pixel^a
Dispersion	1.32 Å/pixel	1.66 Å/pixel^a
Wavelength range^b	5300–8000 Å	5120–8450 Å

[a] After binning the CCDs by 2×2, which is the default.
[b] For a slit at the centre of the field of view.

During run 1 relatively short exposures (typically 1 h) were completed for the 10 clusters of our high-z sample and for one cluster in our intermediate sample. Time lost to bad weather meant that short exposures could not be obtained for the remaining mid-z clusters in this run. For the data acquired, galaxy redshifts were measured when possible. Masks for our run 2 were designed to target established cluster members and additional candidate cluster members for which short exposures were not obtained or a redshift could not be measured due to insufficient signal-to-noise.

In run 2 deep exposures were obtained for the 5 clusters that are the main focus of this paper: Cl 1232 from the mid-z sample and Cl 1040, Cl 1054−11, Cl 1054−12 and Cl 1216 from the high-z sample. The typical exposure time per mask was 2 h at mid-z and 4 h at high-z. In addition short exposures were obtained for a further 8 clusters from the mid-z sample. Seeing was in general subarcsecond and typically varied between 0.″7 and 1.″7.

In run 3 long exposures were obtained for an additional 1–2 masks for the 5 clusters that already had long masks from run 2. This completed the spectroscopic data for these clusters. During run 3 long exposures were obtained for 8 additional clusters, with 2–4 masks per cluster totaling 27 masks. In run 4 the planned long exposures on the high-z sample were completed, and semi-long exposures (1 h per mask) were carried out for clusters from the mid-z sample. These data will be presented in detail in forthcoming papers.

The calibration frames obtained in the 4 runs were as follows. During the bright part of twilight sky flat-field exposures were acquired. During the darker part of twilight calibration stars were observed. Hot stars (spectral type late O to early B) for the telluric absorption correction were observed with a longslit of width 1.″0. Spectrophotometric standard stars for the flux calibration were observed using the FORS2 MOS mode. For our purpose this provided a short "longslit" of width 5.″0 that could be placed anywhere in the field of view. We completed exposures at the extreme left, the centre and the extreme

Table 3. Observing log for the four EDisCS spectroscopic observing runs.

	Exposure time [s]											
	Run 1	Run 2			Run 3				Run 4			
Cluster	m1	m2	m3	m4	m5	m6	m7	m8	m9	m10	m11	Repeats
Mid-z clusters:												
Cl 1018.8−1211	1800		1500		5400	5400	7200					m1–m5; m3–m6
Cl 1059.2−1253		1800			5400	7200	7200					m2–m5
Cl 1119.3−1129		1800							3600	3600	3600	m2–m9
Cl 1202.7−1224		1800							3600	3600	3600	m2–m9
Cl 1232.5−1250*		7200	6360	7200	7200							
Cl 1238.5−1144		1800							1200			m2–m9
Cl 1301.7−1139		1800							3600	3600	3600	m2–m9
Cl 1353.0−1137		2400							3600	3600	3600	m2–m9
Cl 1411.1−1148		1500			10 800	7200	9000					m2–m5
Cl 1420.3−1236		1800							3600	3600	3600	m2–m9
High-z clusters:												
Cl 1037.9−1243	3600				7200	10 800	10 800	10 800				m1–m5
Cl 1040.7−1155*	3600	10 800	14 400	14 400	14 400	14 400						m1–m2
Cl 1054.4−1146*	3600	10 800	14 400	14 400	14 400							m1–m2
Cl 1054.7−1245*	3600	10 800	14 400	14 400	14 400							m1–m2
Cl 1103.7−1245	3600				10 800	10 800			14 400	14 400		m1–m5
Cl 1122.9−1136	3600											
Cl 1138.2−1133	3600				3600	7200	7200	7200				m1–m5
Cl 1216.8−1201*	3600	10 800	14 400	14 400	14 400							m1–m2
Cl 1227.9−1138	3600				10 800	14 400	14 400	14 400				m1–m5
Cl 1354.2−1230	1800				12 600	14 100	15 000	17 400				m1–m5

Notes – m1, m2, ..., m11 denotes mask 1, mask 2, ..., mask 11. The observing run can be deduced from the mask number. A typical observing strategy was to take a short exposure on a cluster in one run, followed in a subsequent run by a longer exposure in which only the spectroscopically confirmed cluster members from the short mask were repeated. Such mask pairs are listed in the column "Repeats". The five clusters marked "$*$" are the main focus of this paper. These are the clusters for which long exposures were obtained in run 2.

right of the field of view, bracketing the range of slit positions and hence wavelength ranges of our MXU galaxy slits.

Bias, screen flat-field and He+Ar+Ne+HgCd comparison arc-lamp exposures were taken by an automatic batch procedure executed after each night of observation. 5 biases, 6 screen flat-field exposures and a single arc-lamp exposure were obtained for each mask and set of stellar observations.

3. Data reduction

Data reduction was completed primarily using IRAF[2]. Specialised algorithms developed for the reduction of similar FORS2 MXU data (Milvang-Jensen 2003) were adopted for several of the reduction steps. In the reduction of the data from run 3, the images from the two CCDs (cf. Table 2) were reduced separately. We describe the data reduction of spectra acquired in runs 1 and 2, and for data from run 3 for the five clusters that are the principle focus of this paper.

Bias subtraction was completed by subtracting a combined bias image. For the run 3 data an overscan level correction was made. Following this cosmic ray hits (hereafter "cosmics") were identified. Different approaches were taken depending on the number of consecutive exposures obtained for a given mask. For the "long masks" typically 4 or 8 exposures of 30 min were available. In this case, cosmics were identified using a method developed by Milvang-Jensen (2003) described in detail in Appendix A.

Single exposures were treated for cosmics using a median filter of dimensions 5 pixels along the dispersion axis and 1 pixel along the spatial axis for data acquired in run 1. Double exposures acquired in run 1 were treated by comparing each frame and taking the minimum value of each corresponding pixel value as that of the output frame. Data obtained in run 2 with 1–3 successive exposures were processed using the LAcosmic algorithm (van Dokkum 2001); a very conservative choice of rejection level was made to prevent removal of skylines; some small cosmics remained and were treated interactively using the IRAF task COSMICRAYS.

The spectra in the upper part of the field curve like a "U" while the spectra in the lower part of the field curve like an upside-down "U". The maximum peak to peak effect was 1.″2 (i.e. 6 px for the 2002 data). This geometrical distortion (S-distortion) was mapped using the edges of the individual "spectra" in the screen flats. Specifically, the screen flats were convolved with a $[-1, 1]$ kernel after which the absolute value was taken. This produced an image in which the edges of the spectra show up as positive features (the convolution is equivalent to moving the image downwards by 1 pixel and subtracting it from itself.) These features were then used to map the distortion. All frames (science, flat fields and arcs) were

[2] IRAF is distributed by the National Optical Astronomy Observatories, which are operated by the Association of Universities for Research in Astronomy, Inc., under cooperative agreement with the National Science Foundation.

then corrected for the distortion. This created spectra parallel to the *X* axis.

For each mask the combined screen flat exposures were used to construct two types of flat field: a pixel-to-pixel flat field and a flat field in which no normalisation was made in the wavelength direction. The pixel-to-pixel flat was constructed by normalising each row using a 20-piece cubic spline, i.e. by removing the wavelength dependence caused by the combined effect of the SED of the screen flat lamp and the transmission function of the system (mirrors, grism, CCD). The pixel-to-pixel flat field was applied to the corresponding science frame. In this way the original counts are preserved, allowing the photon noise to be readily computed. The second type of flat field was constructed as follows. The combined screen flat image for the given mask was cut up and each slit spectrum wavelength calibrated. The slits in the masks were in general at different *x*-positions and the slit closest to the centre in the *x*-direction was located. Only the overall level in the screen flat spectrum was normalised, leaving the wavelength dependence intact. The normalisation constant was chosen to give a level of one at a reference wavelength of 6780 Å, which is central wavelength of the grism according to the manual. This normalisation constant was used to normalise all other screen flat spectra for the mask. These flat field spectra were used to create a second set of science frames required for the flux-calibration of science spectra (cf. below).

Since the frames had been geometrically rectified, the individual slitlet spectra within each CCD frame were identified by specifying the *Y* coordinate of the lower and upper edges of the spectra positions. The slitlet edges were automatically defined as the points where the intensity had dropped to 95% of the maximum level within the given slitlet screen flat spectrum. Both science and arc frames were cut. From this point on, the data reduction was identical to the reduction of longslit data.

For each slitlet a 2D wavelength calibration was established and applied using the corresponding cut arc spectrum and standard IRAF tasks. The rms of the fits was typically 0.05 Å. Typically 30–40 arc lines well distributed over the wavelength range were used.

Sky-subtraction was performed by first creating one-dimensional spatial profiles for each cut wavelength-calibrated science spectrum. Each profile was examined and suitable intervals along the spatial axis for which a fit to the sky level were decided. The sky was modelled as a constant at each pixel in the wavelength direction.

One-dimensional spectra were extracted using the IRAF task *apall*. The extraction aperture was chosen to be the *FWHM* of the spatial profile and within each aperture the flux was summed.

The longslit spectra of the hot stars were reduced following a similar procedure to that of the MXU data. The issue of the two types of flat fields is irrelevant here, since the extracted 1D spectra were normalised to unity in the continuum. In the blue part of the spectrum, where these stars have intrinsic spectral features, the level was set to unity. The resulting telluric absorption correction spectrum was scaled and applied to the galaxy spectra.

As mentioned, slit spectra of the spectrophotometric standard stars were taken at three positions: right, centre and left, covering three wavelength ranges: extreme blue, central and extreme red, respectively. The central spectrum has a substantial overlap with the two other spectra. However, when only the pixel-to-pixel flat field was applied, within the overlap regions the spectra had quite different shapes. We attributed this to the grism having a spectral response that depends on the position (angle) within the field of view. After the three spectra were divided by the screen flat field in which spectral shape was left in (cf. above), the spectra *did* match up and could be combined to form a single spectrum covering a wavelength range bracketing that for all galaxy spectra. From this spectrum the sensitivity function was derived and applied to the galaxy spectra that had been reduced using the same type of flat field. We thus use the fact that the position dependent spectral response of the grism is recorded both in the individual galaxy and star spectra and in the corresponding screen flat spectra, and when the former is divided by the latter, the spectral response of the grism cancels out, as long as the SED of the lamp stays constant.

4. Cluster and galaxy redshifts

4.1. Galaxy redshifts

We present representative spectra for cluster members of the high-redshift cluster Cl 1216 (Fig. 1) and the intermediate-redshift cluster Cl 1232 (Fig. 2). We show the spectrum for the brightest cluster galaxy and spectra for an additional 5 progressively fainter galaxies.

Spectroscopic galaxy redshifts were measured using emission lines where possible, in particular the [OII]λ3727 line, or the most prominent absorption lines, e.g. Calcium K and H lines at 3934 Å and 3968 Å. Errors for galaxy redshifts were calculated using repeat galaxy observations acquired during spectroscopic runs 1 and 2. Our typical galaxy redshift error was approximately 0.0003 (90 $\mathrm{km\,s^{-1}}$), corresponding to 50 and 60 $\mathrm{km\,s^{-1}}$ rest frame at $z = 0.8$ and $z = 0.5$ respectively. We compared our redshift measurements with values determined using the Fourier Correlation Quotient method of Bender (1990) and found a typical intrinsic uncertainty of 0.00011 (18 $\mathrm{km\,s^{-1}}$ at $z = 0.8$ rest frame; 22 $\mathrm{km\,s^{-1}}$ at $z = 0.5$ rest frame).

Throughout this paper, a galaxy is considered to be a member if its redshift is within $3\sigma_{\mathrm{cluster}} = \pm(3\times\sigma_{\mathrm{cluster}})$ of the cluster redshift (cf. expression (3)), where $\sigma_{\mathrm{cluster}}$ is the cluster velocity dispersion presented in Sect. 5.

4.2. The spectroscopic catalogue

We present the catalogue of spectroscopic observations of 5 EDisCS clusters. The tables are available in electronic form at the CDS. We note that entries for repeated observations are included in these tables. The format of each table is illustrated in Table 4. The tables provide the galaxy ID in Col. 1; object RA and Dec (J2000) in Cols. 2 and 3; *I*-band magnitude for an aperture of radius 1″ in Col. 4; a spectroscopic redshift in Col. 5; a membership flag in Col. 6; and a "targeting" flag in Col. 7.

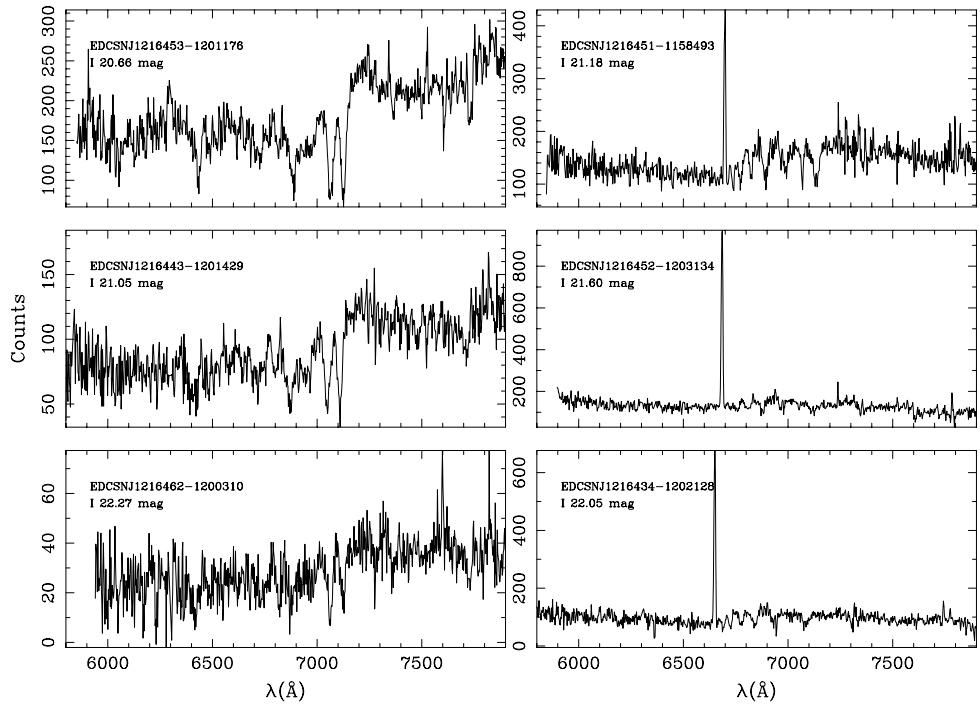

Fig. 1. Example spectra (2 pixel binning) of galaxies in the cluster Cl 1216 at $z = 0.79$. Galaxy IDs and 1″ aperture *I*-band magnitudes are given for each spectrum. The bright emission line [OII]λ3727 (clearly visible in the right-hand panel figures) was used to determine the galaxy redshift where possible; otherwise the redshift was measured using the Calcium H and K lines (clearly visible in the interval 7000–7200 Å of the left-hand panel figures). All spectra are presented after correction for telluric absorption and before flux calibration.

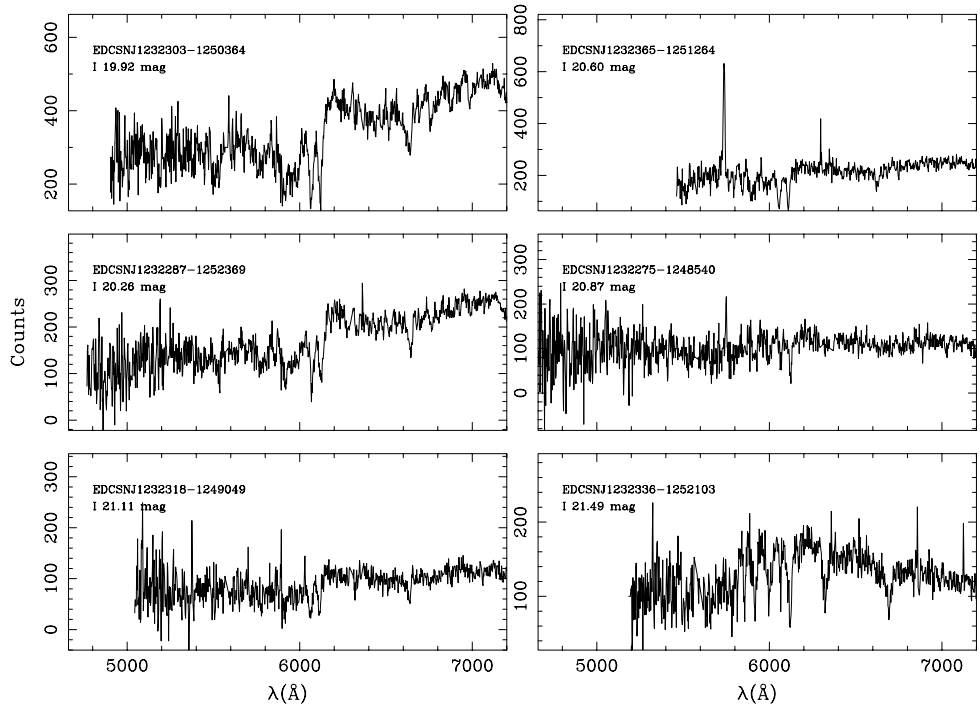

Fig. 2. Example spectra (2 pixel binning) of galaxies in the cluster Cl 1232 at $z = 0.54$. Galaxy IDs and 1″ aperture *I*-band magnitudes are given for each spectrum. The bright emission line [OII]λ3727 (clearly visible in the two top right-hand panel figures) was used to determine the galaxy redshift where possible; otherwise the redshift was measured using the Ca H and K lines (clearly visible in the interval 6000–6200 Å of the left-hand panel figures). All spectra are presented after correction for telluric absorption and before flux calibration.

In Col. 1, a colon (:) indicates that multiple spectra were extracted for a single photometric object. Two redshifts have an associated ID with a colon: these two cases are shown in the example table (Table 4). Our HST ACS image indicates that we are seeing two galaxies in projection. 3 galaxies were not included in the final versions of our photometric catalogues due

Table 4. Example spectroscopic catalogue.

EDisCS object	RA	Dec	I-band magnitude	Spectroscopic redshift	Membership flag	Targeting flag
EDCSNJ1054316-1147400	10:54:31.62	−11:47:40.0	21.249	0.6908	1	1
EDCSNJ1054254-1147523:	10:54:25.38	−11:47:52.3	21.380	0.6977	1	1
EDCSNJ1054254-1147523:	10:54:25.38	−11:47:52.3	21.380	0.8385	0	3
EDCSNJ1054260-1148009	10:54:26.02	−11:48:00.9	21.815	0.6802	3	1
EDCSXJ1054338-1145437	10:54:33.81	−11:45:43.7	22.90	0.6649	0	1
EDCSNJ1054494-1243321	10:54:49.36	−12:43:32.1	22.947	0.6864::	0	1
EDCSNJ1054504-1243410	10:54:50.42	−12:43:41.0	21.471	0.7309	1B	1
EDCSNJ1054504-1243259	10:54:50.44	−12:43:25.9	23.875	0.225:	0	3
EDCSNJ1216431-1158113	12:16:43.11	−11:58:11.3	22.503	1.0579:	0	1
EDCSNJ1232389-1252170	12:32:38.95	−12:52:17.0	21.523	0.6809	0	2
EDCSNJ1232285-1254057	12:32:28.54	−12:54:05.7	17.873	0.0000	0	4
EDCSNJ1232322-1253003	12:32:32.17	−12:53:00.3	20.824	9.9999	0	1

to changes in object identification criteria. For these galaxies an empirical ID has been constructed using the galaxy RA and Dec coordinates, and a prefix of X instead of N; I-band magnitudes are taken from the version of our photometric catalogues used to prepare the spectroscopic observations.

In Col. 5, a colon indicates a redshift with a higher than average uncertainty, while a double colon (::) indicates a doubtful redshift. $z = 0.0000$ corresponds to stars, and $z = 9.9999$ is used where a redshift could not be determined. The uncertainty in the redshift estimate of the spectra listed with a colon was mostly due to a lower than usual S/N or sky features affecting the lines most suitable for the redshift measurements. This resulted in a less precise identification of the line centres. While the approximate redshift is confirmed by several lines in these cases, the exact redshift value cannot be established with the same accuracy as for the secure redshifts. Those cases with a double colon (6 spectra in total) are all low S/N spectra, where the redshift estimate had in general to be based on one single line in emission, whose redshift could not be confirmed by any other emission or absorption line in the spectrum. In all of these cases the reality of the observed line in emission was verified by inspecting the 2D spectra. Only for one spectrum marked by a double colon was the redshift estimate based on the presence of a clear break in the continuum intensity, but no specific lines were identified without doubt due to the low S/N.

The numeric membership flag in Col. 6 is "1" for cluster members (within $3\sigma_{\rm cluster}$ of the cluster redshift); "2" and "3" for galaxies at $3\sigma_{\rm cluster}$ to $4\sigma_{\rm cluster}$ and $4\sigma_{\rm cluster}$ to 10σ from the cluster redshift, respectively, that can be considered members of a supercluster region; and "0" in all other cases of fore- and back-ground non-members. The cluster Cl 1054-12 has a secondary structure $7\sigma_{\rm cluster}$ away in redshift from the main structure (see Sect. 5 and Table 5). In this case a membership flag is listed both for the main cluster Cl 1054-12A ("1A", "2A", "3A", with meaning as above) and for the secondary structure Cl 1054-12B ("1B", "2B", "3B"). Where a galaxy can have, for example, both a "3A" and "1B" flag, a "1B" flag has been assigned.

Column 7 indicates whether the galaxy was a selected spectroscopic target, hence was targeted for spectroscopy as a possible member of the cluster (flag = 1); if it was observed but believed to be a "field" (non-cluster) galaxy based on the photometric-redshift criteria (flag = 2); if it is a galaxy that happened to fall into the slit together with a targeted galaxy (flag = 3); and if it was targeted as a star to aid acquisition (flag = 4). As described below, this information can be used to assess the success of our observing strategy and the effects of the selection criteria adopted.

Table 5. Cluster member redshifts, velocity dispersions and numbers for 5 EDisCS clusters. The cluster name is indicated in Col. 1. In Col. 2 we provide the cluster redshift. In Col. 3, cluster velocity dispersions ($\sigma_{\rm cluster}$) are shown together with their errors in km s^{-1}. In Col. 4 we indicate the number of cluster members considered in the measurement of cluster velocity dispersion (see Sect. 5.2). In Col. 5 the number of cluster members is revised to include members with redshifts of higher than average uncertainty and doubtful redshifts (see Sects. 4.2 and 5.2).

Cluster name	$z_{\rm cluster}$	$\sigma_{\rm cluster} \pm \delta\sigma_{\rm cluster}$	No. of members I	No. of members II
(1)	(2)	(3)	(4)	(5)
Cl 1040	0.7043	$418\ ^{+55}_{-46}$	30	30
Cl 1054–11	0.6972	$589\ ^{+78}_{-70}$	48	49
Cl 1054–12	0.7498	$504\ ^{+113}_{-65}$	35	36
Cl 1216	0.7943	$1018\ ^{+73}_{-77}$	66	67
Cl 1232	0.5414	$1080\ ^{+119}_{-89}$	52	54

4.3. Success rate, completeness and potential selection biases

It is important to establish a posteriori if the criteria used to select our spectroscopic targets have biased the final spectroscopic cluster member dataset. As described in Sect. 2.1, to maximise the number of targeted cluster members and avoid rejection of possible cluster galaxies, we adopted conservative criteria based on our photometric redshifts. To recap, our selection criteria have rejected between 30% and 50% of the objects in the full photometric catalogues of our high redshift clusters, and approximately 35% of objects in the catalogue of the ∼0.5 cluster (Cl 1232).

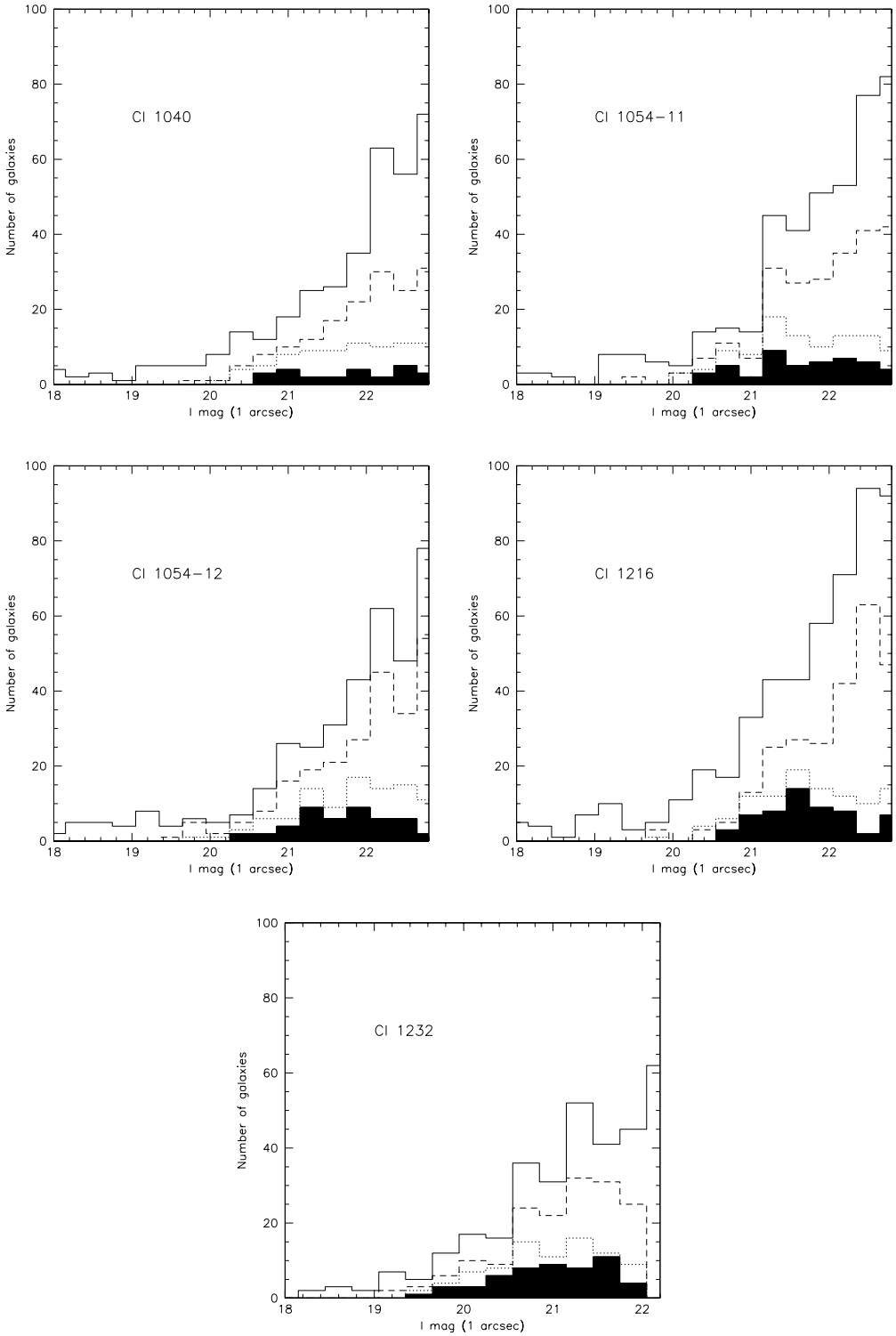

Fig. 3. Magnitude distributions for our 5 clusters. The solid, largest histogram represents the magnitude distribution of all objects detected by SExtractor in the EDisCS fields (the full photometric catalogue in the area of sky sampled by the 2002 spectroscopy). The dashed histogram is the distribution of objects that were retained as potential spectroscopic targets within the area of sky sampled by the 2002 spectroscopy after applying the selection criteria described in Sect. 2.1. The magnitude distribution of selected spectroscopic targets for which a spectrum was obtained is shown as a dotted histogram, while that of all selected spectroscopic targets confirmed to be cluster members is shown as a filled histogram.

The solid and dashed histograms in Fig. 3 present the magnitude distribution of all objects detected by SExtractor in the EDisCS FORS2 field (i.e. our full photometric catalogues) and of potential spectroscopic targets decided after applying the selection criteria described in Sect. 2.1. The same plot illustrates the magnitude distribution of selected spectroscopic targets for

which a spectrum was acquired (dotted histogram), and of selected spectroscopic targets which are cluster members according to their spectroscopic redshift (filled histogram).

Figure 3 indicates that our membership success rate has been high. The fraction of objects targeted as cluster members and then confirmed to be members is approximately 75% in Cl 1232, 60% in Cl 1216, 50% in Cl 1054–12 and Cl 1054–11, and 30% in Cl 1040[3]. The spectroscopic cluster catalogues typically include spectra for approximately 20% of all potential spectroscopic targets (∼25% in Cl 1216 and 35% in Cl 1232). Redshift measurements were obtained for 91–98% of objects targeted as cluster members for a given set of cluster observations. In cases where the spectrum did not yield a redshift the object was either of very low S/N spectra and among the faintest of the sample (generally fainter than $I = 22.5$), or relatively bright objects ($I \sim 20$ or brighter) with a featureless spectrum that, judging from the shape of the red continuum, most probably are at a redshift much lower than our clusters.

We recall that due to geometrical constraints in our mask design, 65 slits were assigned to objects *rejected* by our cluster member selection criteria. Importantly *none* of these objects was found to be a cluster member galaxy. Thus our adopted selection criteria have neither rejected real cluster members nor biased our spectroscopic catalogue of cluster members relative to a purely I-band selected sample (Sect. 2.1).

5. Cluster redshifts and velocity dispersions

In this section we present galaxy redshift histograms (Sect. 5.1) and cluster velocity dispersion measurements (Sect. 5.2) for our 5 EDisCS clusters.

5.1. Redshift histograms

In Fig. 4 we show redshift histograms obtained from the long spectroscopic observations of each cluster. The redshift distribution is clearly dominated by one main peak in redshift space at the cluster redshift. For Cl1054–12, a secondary structure is evident very close to the main cluster peak. For Cl1232 there appears to be substructure in its velocity histogram. It is not immediately obvious that these structures are spatially offset from each other on the sky (see Sect. 6).

5.2. Cluster velocity dispersions

We present the measurement of cluster velocity dispersion ($\sigma_{\rm cluster}$) for each cluster.

A widely adopted estimator for cluster velocity dispersions is the biweight statistic discussed by Beers et al. (1990) (hereinafter BFG90). For a typical dataset of 20 to 50 galaxies BFG90 show that the *biweight scale estimator* is a robust estimator of distribution spread and demonstrate its insensitivity to outlying points.

[3] When computing the success rate, galaxies in Cl 1054–12A and Cl 1054–12B have been considered together, since the separation in redshift (0.0195) is far too small to be separated by any photometric-redshift technique. The lower success rate in Cl 1040 is due to a higher contamination from back- and fore-ground galaxies.

For each cluster, we estimate $\sigma_{\rm cluster}$ using biweight statistics: $\sigma_{\rm cluster}$ is taken to be the biweight estimator of scale for an input redshift list and its asymmetric errorbars are estimated from Monte Carlo bootstrap simulations (BFG90). Spectroscopic redshift measurements of uncertain quality (with a colon or double colon in Table 4) were rejected when estimating these quantities.

An initial estimate of mean cluster redshift ($z_{\rm init}$) was made using redshifts judged to belong to the main peak of each cluster redshift histogram.

Redshifts z_i within an interval of:

$$(z_{\rm init} - 0.015) \leq z_i \leq (z_{\rm init} + 0.015) \quad (1)$$

were used to obtain a first estimate of $\sigma_{\rm cluster}$. To transform to the cluster rest-frame, redshifts were multiplied by the speed of light, c, to create recessional velocities $v_{{\rm init}_i}$; the median of all these recessional velocities ($v_{\rm median}$) was then found, and velocities in the cluster reference frame were taken to be:

$$v_{{\rm rest}_i} = (v_{{\rm init}_i} - v_{\rm median}) \Big/ \left(1 + \frac{v_{\rm median}}{c}\right). \quad (2)$$

An improved estimate of $\sigma_{\rm cluster}$ was taken to be the biweight estimator of scale for all these $v_{{\rm rest}_i}$. Its uncertainty was estimated as the 1-σ bootstrap confidence interval. Next a 3-σ clipping was performed i.e. all input $v_{{\rm rest}_i}$ outside the interval:

$$-(3 \times \sigma_{\rm cluster}) \leq v_{{\rm rest}_i} \leq (3 \times \sigma_{\rm cluster}) \quad (3)$$

were rejected and the measurement of $\sigma_{\rm cluster}$ was repeated on the remaining velocity set. This step was iterated until expression (3) held true for all input $v_{{\rm rest}_i}$. The uncertainty of the final $\sigma_{\rm cluster}$ measurement was again estimated as the 1-σ bootstrap confidence interval. We define *cluster members* to be those galaxies for which expression (3) holds after the final iteration.

In Table 5 we give the results of this exercise. The *cluster redshift* given here, $z_{\rm cluster}$, is the median redshift of all *cluster members*.

6. Cluster substructure

Figure 5 presents zoomed-in velocity histograms for our five clusters using 500 $\rm km\,s^{-1}$ bins. In each panel, the red skeletal arrow marks the median recessional velocity of the cluster members (i.e. the cluster redshift defined above), and the blue filled arrow marks the recessional velocity of the BCG. A Gaussian centred at the median recession velocity and of width corresponding to the cluster velocity dispersion is plotted for reference. The velocity histograms show different levels of deviation from a Gaussian, providing evidence of complex dynamical structure and suggesting that some clusters are far from equilibrium. In this section, we assess substructure within each cluster first based on XY position maps of cluster members for different redshift intervals (Sect. 6.1) and then using the Dressler-Shectman test (Sect. 6.2).

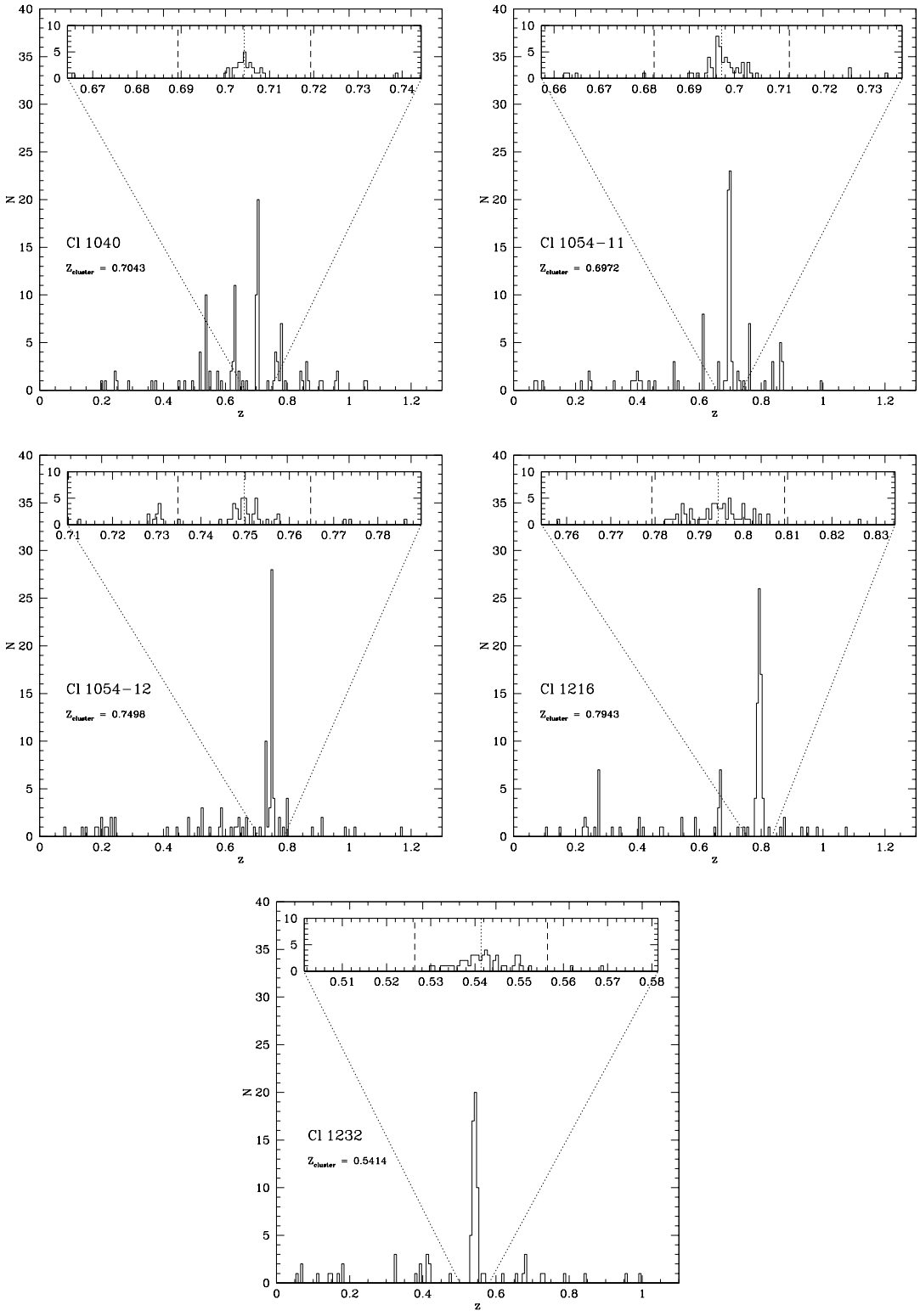

Fig. 4. Redshift histograms based on the long spectroscopic exposures of our 5 EDisCS clusters. An inset panel in each plot shows a zoomed histogram for the redshift interval $z_{\rm cluster} - 0.04 \leq z \leq z_{\rm cluster} + 0.04$, where the cluster redshift $z_{\rm cluster}$ is indicated by a dotted line. Dashed lines indicate the interval $z_{\rm cluster} - 0.015 \leq z \leq z_{\rm cluster} + 0.015$. Redshift bins are 0.00625 (1874 km s^{-1} observed frame) for the main plot and 0.000625 for the inset plot. In all cases the redshift distribution is dominated by one peak at the cluster redshift.

6.1. XY position diagrams

In Fig. 6 we present *XY* position maps for galaxies within the *I*-band magnitude range for which our spectroscopy was completed and we consider as possible cluster members on the basis of their photo-z's. Objects identified as non-members from our spectroscopy are excluded. For each cluster the position of the BCG is indicated by both a black cross and a colour

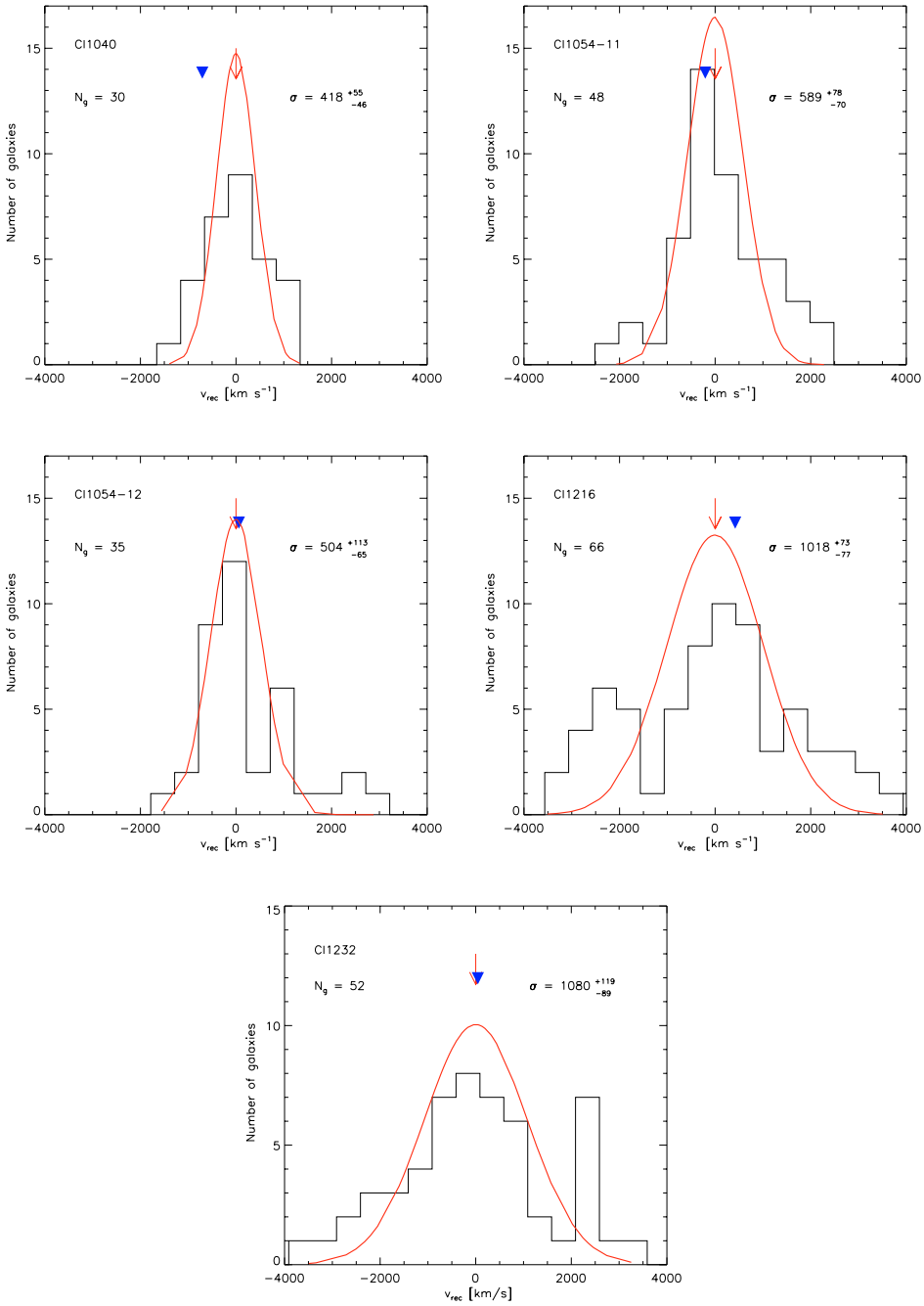

Fig. 5. Velocity histograms for the five clusters discussed in this paper. The red skeletal arrows mark the median recessional velocity of all spectroscopically-confirmed cluster members, while the blue filled arrows mark the recessional velocity of the BCGs. The red Gaussians correspond to the measured cluster velocity dispersion.

symbol. We study cluster structure in three dimensions by subdividing cluster members into three groups corresponding to different redshift intervals. Members indicated by green circles are all galaxies with redshift z_i in the interval

$$(z_{\rm cluster} - z_\sigma) \leq z_i \leq (z_{\rm cluster} + z_\sigma)$$

where $z_\sigma = \frac{\sigma_{\rm cluster}}{c} \times (1 + z)$ is the redshift interval corresponding to the cluster velocity dispersion $\sigma_{\rm cluster}$ presented for each cluster in Sect. 5.2.

Similarly blue triangles indicate cluster members with redshift z_i such that

$$z_i < (z_{\rm cluster} - z_\sigma)$$

and red squares, cluster members with redshift z_i such that

$$z_i > (z_{\rm cluster} + z_\sigma).$$

For Cl 1054–12, some clustering of galaxies indicated by red and green symbols may be present close to the cluster centre. For Cl 1216, there are two clear substructures, one given by galaxies with red and green symbols at cluster centre and

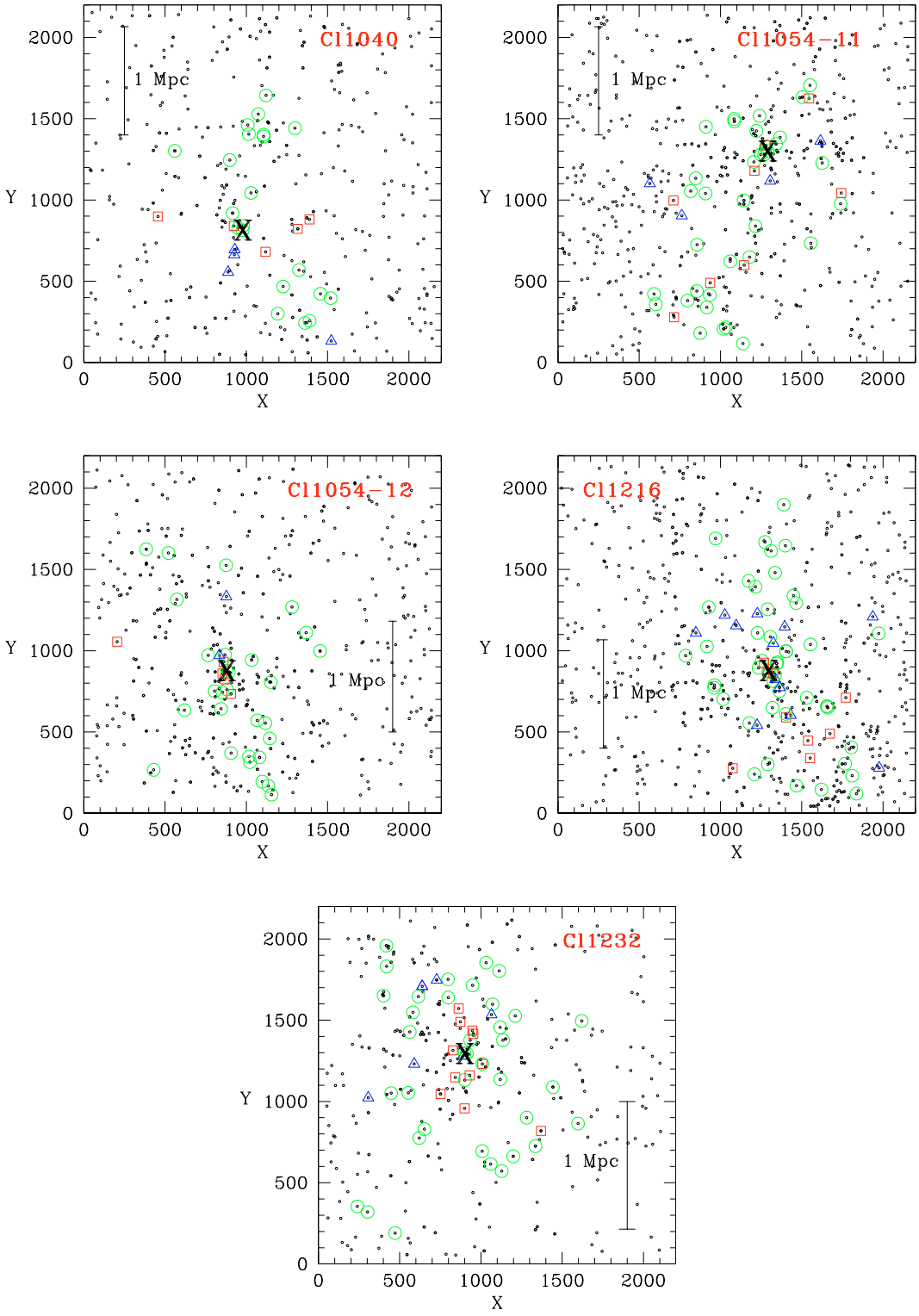

Fig. 6. Plots of galaxy positions. Axis scales are in units of CCD pixels (0.″2/pixel). The cluster name is indicated at the top of each plot. Large open symbols show the positions of cluster members: green circles indicate galaxies within ±one z_σ of the cluster redshift, red squares indicate galaxies whose redshift is more than one z_σ higher than $z_{\rm cluster}$, while blue triangles indicate galaxies whose redshift is lower than $z_{\rm cluster}$ by more than one z_σ where z_σ is the redshift interval corresponding to the cluster velocity dispersion in observed frame. Small circles are galaxies without spectroscopy selected from our I-band photometric catalogues to be possible cluster members. The position of the brightest cluster galaxy (BCG) is indicated by a black cross symbol. A physical distance of 1 Mpc (assuming $\Omega = 0.3$, $\Lambda = 0.7$ and $h = 0.7$) is shown in each plot.

another less concentrated structure offset towards low X and high Y (northeast of the BCG), shown mainly by blue symbols. For Cl 1232 an extended substructure indicated mainly by red symbols is clear towards the cluster centre. No clear spatial segregation is apparent for any redshift intervals in Cl 1054–11 and Cl 1040.

6.2. The Dressler-Shectman test

More robust evidence for substructure requires its significance and its properties to be quantified. Dressler & Shectman (1988) devised a statistical test that uses galaxy velocities and positions to constrain cluster substructure in three dimensions. The principle of the method is the following. Starting from a list of cluster members with measured positions and velocities, for each galaxy one finds the ten listed nearest neighbours on the sky. The local mean velocity and velocity dispersion are computed from this sample of 11 galaxies. These quantities, defined for each galaxy in the list, are then compared to the global cluster mean and velocity dispersion using the parameter δ defined to be:

$$\delta^2 = \frac{11}{\sigma^2} \times \left[(\bar{v}_{\rm local} - \bar{v})^2 + (\sigma_{\rm local} - \sigma)^2 \right] \quad (4)$$

where σ and $\bar{v}$ are the cluster velocity dispersion and the cluster redshift respectively, as given for each cluster in Sect. 5, while $\sigma_{\rm local}$ and $\bar{v}_{\rm local}$ are the quantities defined locally for each galaxy.

Dressler & Shectman (1988) define the cumulative deviation Δ as the sum of the δ for all the cluster members $N_{\rm g}$. Note that the Δ statistic is similar to a χ^2: if the cluster velocity distribution is close to Gaussian and local variations are just sampling fluctuations, then Δ will be of the order of $N_{\rm g}$.

This technique does not allow a direct identification of galaxies belonging to a detected substructure. The position of substructures can however be identified by plotting the distribution of the galaxies on the sky using symbols whose size is proportional to the parameter δ, thus quantifying the local deviation from the global kinematics of the cluster. Such an analysis is shown for our 5 clusters in Fig. 7. In each panel, the size of the symbols is proportional to $e^{\delta/2}$ and a cross symbol marks the position of the BCG. The circle symbols are coloured according to the criteria described in Sect. 6.1. To first order the presence of many large circles in a given area should correspond to substructure, i.e. a correlation both spatially and kinematically of separate structures. Our plots in Fig. 7 indicate that complex dynamical structure may be present for all clusters although significant substructuring is detected for only Cl 1216 and Cl 1232.

The Δ statistic can be used to give a quantitative estimate of the significance of the putative substructure. We have computed a set of 1000 Monte Carlo simulations for each cluster by randomly re-shuffling the velocities of the cluster members. This removes any significant 3D substructure. The statistical significance of the observed substructure can then be quantified by the fraction P (Dressler & Shectman 1988) of the simulations that yield Δ values larger than the observed one where a *small* value of P corresponds to a *high* significance. In Table 6 we list the number of spectroscopic members, the measured Δ statistic, and the measure of substructuring significance P.

Table 6. Number of spectroscopic members ($N_{\rm g}$), value of the Δ statistic, and the measure of substructuring significance P, for each of the clusters used in the present analysis (see text for details).

Cluster name	$N_{\rm g}$	Δ	P
Cl 1040	30	55.11	0.08
Cl 1054–11	48	71.77	0.64
Cl 1054–12	36	108.87	0.14
Cl 1216	67	135.58	0.05
Cl 1232	54	96.57	0.01

For two of our clusters (Cl 1232 and Cl 1216), substructure is detected by the DS test with more than 95% confidence. This agrees with the spatial segregation of galaxies in different velocity intervals seen in Fig. 6 and with the existence of peaks redward (Cl 1232) or blueward (Cl 1216) of the cluster redshift in the velocity histograms (Fig. 5). In Cl 1232 the redshifted galaxies are mainly projected near the cluster centre, while in Cl 1216 the blue-shifted galaxies are offset North-East of the BCG. In two clusters (Cl 1040 and Cl 1054–12), substructure appears to be present, based on the DS probability, but the available data do not yet provide firm statistical evidence. No evidence for substructure is found in Cl 1054–11. Interestingly, the two clusters with the clearest substructure are the ones with the largest velocity dispersions, both exceeding 1000 km s^{-1}. At these redshifts, equilibrium clusters with such high velocity dispersions are rare according to the standard hierarchical ΛCDM scenario (e.g. Eke et al. 1996). The substructure analysis suggests that both clusters have considerable depth in redshift, indicating that they may still be collapsing along or close to the line-of-sight. One should therefore be extremely cautious when using their measured velocity dispersions to estimate their masses. Such non-virialised structures are not unexpected in ΛCDM models (Evrard et al. 2002).

7. Summary

We present spectroscopic observations of 5 clusters, 4 at redshift of 0.7–0.8, 1 at redshift $\sim$ 0.5, completed as part of the ESO Distant Cluster Survey (EDisCS). We demonstrate how our target selection strategy has maximised our cluster member dataset. We present spectroscopic catalogues of positions, redshifts and I-band magnitudes for galaxies observed in the fields of our clusters. We have acquired data for 236 cluster members and the number of cluster members per cluster ranges between 30 and 67. Our spectroscopic success rate at targeting members was 30–75%, averaging 50%. Our cluster velocity dispersions measured using a robust biweight estimator range from 400 to 1100 km s^{-1}. We find significant evidence for substructure in two clusters, one at $z \sim 0.79$ and the other at $z \sim 0.54$. Both clusters have velocity dispersions exceeding 1000 km s^{-1} and are unlikely to be fully virialised: their velocity dispersions may therefore not provide a robust estimate of their mass. The properties of our 5 EDisCS clusters cover a range of

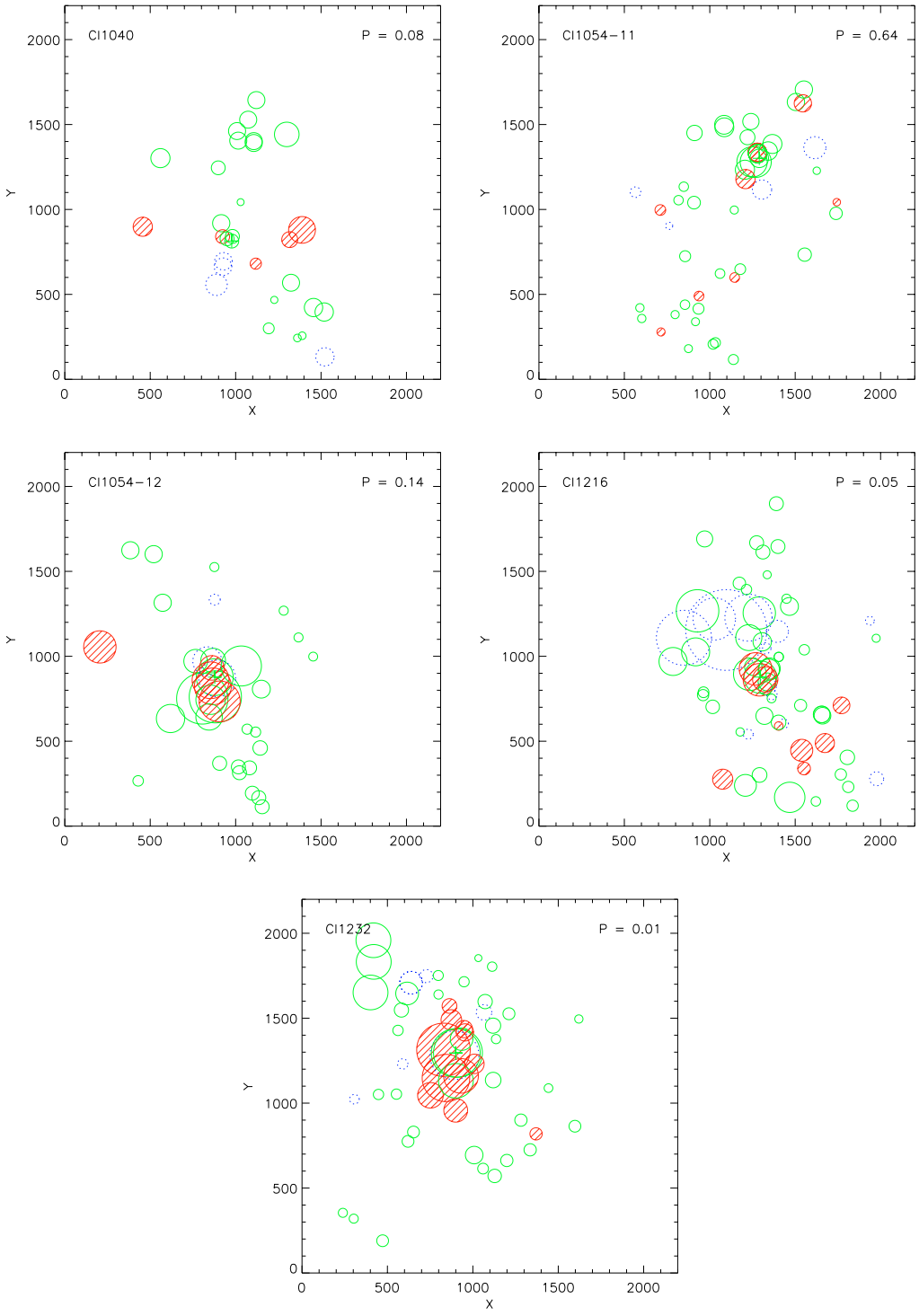

Fig. 7. Dressler-Shectman (DS) analysis. The radii of the plotted circles is equal to $e^{\frac{\delta}{2}}$ where δ is the DS measurement of local deviation from the global velocity dispersion and mean recession velocity. Green circles marked by a solid line indicate galaxies with redshift z_i such that $(z_{\rm cluster} - z_\sigma) \leq z_i \leq (z_{\rm cluster} + z_\sigma)$, red circles indicated by hashed areas, galaxies with $z_i > (z_{\rm cluster} + z_\sigma)$, and blue circles indicated by a dotted line, $z_i < (z_{\rm cluster} - \sigma_{\rm cluster})$. The measure of substructuring significance P is provided at the top right hand corner of plots for each cluster.

velocity dispersions, richness and substructuring typical of our survey. Our full spectroscopic dataset will allow a comprehensive study of galaxy evolution as a function of redshift and cluster environment.

Acknowledgements. We thank Timothy Beers, Andrea Biviano and Alan Dressler for helpful discussions. We thank the staff of the ESO Very Large Telescope observatory, Paranal, Chile, for their help and support before, during and after observations. The anonymous referee is gratefully thanked for a constructive report which improved the quality of the final manuscript. C.H. acknowledges the use of the program ROSTAT. C.H. and B.M.P. gratefully acknowledge the grant support of the Italian National Research Centre, grant number CNRG008871, and a grant from the "Fondo per gli Investimenti della

Ricerca di Base" of the Italian Ministery of Education, University and Research (grant RBAU018Y7E). G.D.L. thanks the Alexander von Humboldt Foundation, the Federal Ministry of Education and Research, and the Programme for Investment in the Future (ZIP) of the German Government for financial support. R.P.S. and G.R. acknowledge the support by the Deutsche Forschunggemeinschaft (DFG), SFB 375 (Astroteilchenphysik).

Appendix A: Cosmic ray removal algorithm

For the "long masks" typically 4 or 8 exposures of 30 minutes were available and the following method was used (Milvang-Jensen 2003; Milvang-Jensen & Aragón-Salamanca, in preparation). Consider the example of 8 exposures. To be able to flag deviating values among the 8 values available at a given pixel position we must calculate the expected standard deviation (hereinafter "sigma") in the absence of cosmics. One estimate of sigma can be computed from the median using the CCD noise model (photon noise and read-out noise). Since the numerous sky lines have large intrinsic intensity variations this sigma can however significantly underestimate the actual frame-to-frame variation. The sigma must therefore be measured from the data. The number of pixels affected by cosmics in a given 30 minute exposure is approximately 0.2%. It follows that for a given pixel position at most 2 values are expected to be affected by cosmics, and thus the lowest 6 values can be used to compute a sigma. As a statistic we used the RMS (run 2) or the MAD (mean absolute deviation from the sample mean) (run 3); the results were found to be similar. This sigma estimate is biased low with respect to the intrinsic value (still in the absence of cosmics). The exact factor was found from simulations using a normal parent distribution. The estimates were then multiplied by this factor to give a "measured" sigma estimate, e.g. $\sigma_{\rm meas.} \equiv 1.79 \cdot {\rm MAD}$ (lowest 6 of 8). This estimate incorporates the large variations due to the varying strength of the sky lines, while giving a value close to that predicted by the CCD noise model in regions of the spectra not affected by sky lines. However, due to small number statistics ($\sim \sqrt{6}$ uncertainty) the measured sigma can occasionally be too small. Therefore, the final sigma was taken to be the maximum of the measured sigma and the CCD noise model sigma. Cosmics in the individual frames could now be identified as values exceeding the median image by more than N sigma. The factor N was chosen manually on a frame by frame basis in such a way that very few good (i.e. non-cosmic) pixels were flagged. Usually $N = 4-5$ worked. If however a series of 8 (say) mask exposures was started at the beginning of the night, sky lines in the first exposures could be much brighter than in the remainder in a way not predictable using the measured sigma: in this case a larger threshold N was required. For run 2 the cosmic maps were used to clean the individual exposures using linear interpolation within each frame. Following this the exposures were combined (i.e. averaged). For run 3 the cosmic masks were used to exclude cosmics when combining the frames. It should be noted that the stability of FORS2 is excellent and the shift in wavelength and spatial direction during 4 h (8 exposures) of uninterrupted observations is small ($\lesssim$0.5 pixel), allowing frames to be combined without shifts.

References

Abell, G. O. 1958, ApJS, 3, 211
Aragón-Salamanca, A., Baugh, C. M., & Kauffmann, G. 1998, MNRAS, 297, 427
Balogh, M. L., Morris, S. L., Yee, H. K. C., Carlberg, R. G., & Ellingson, E. 1997, ApJ, 488, L75
Beers, T. C., Flynn, K., & Gebhardt, K. 1990, AJ, 100, 32
Bender, R. 1990, A&A, 229, 441
Bolzonella, M., Miralles, J.-M., & Pelló, R. 2000, A&A, 363, 476
Borgani, S., Girardi, M., Carlberg, R. G., Yee, H. K. C., & Ellingson, E. 1999, ApJ, 527, 561
Bruzual A., G., & Charlot, S. 1993, ApJ, 405, 538
Calzetti, D., Armus, L., Bohlin, R. C., et al. 2000, ApJ, 533, 682
Coleman, G. D., Wu, C.-C., & Weedman, D. W. 1980, ApJS, 43, 393
Couch, W. J., Ellis, R. S., MacLaren, I., & Malin, D. F. 1991, MNRAS, 249, 606
Couch, W. J., & Sharples, R. M. 1987, MNRAS, 229, 423
Danese, L., de Zotti, G., & di Tullio, G. 1980, A&A, 82, 322
Dressler, A., & Shectman, S. A. 1988, AJ, 95, 985
Dressler, A., Smail, I., Poggianti, B. M., et al. 1999, ApJS, 122, 51
Eke, V. R., Cole, S., & Frenk, C. S. 1996, MNRAS, 282, 263
Evrard, A. E., MacFarland, T. J., Couchman, H. M. P., et al. 2002, ApJ, 573, 7
Fisher, D., Fabricant, D., Franx, M., & van Dokkum, P. 1998, ApJ, 498, 195
Geller, M. J., & Beers, T. C. 1982, PASP, 94, 421
Gioia, I. M., Maccacaro, T., Schild, R. E., et al. 1990, ApJS, 72, 567
Gladders, M. D., & Yee, H. K. C. 2000, AJ, 120, 2148
Gonzalez, A. H., Zaritsky, D., Dalcanton, J. J., & Nelson, A. 2001, ApJS, 137, 117
Gonzalez, A. H., Zaritsky, D., Simard, L., Clowe, D., & White, S. D. M. 2002, ApJ, 579, 577
Gunn, J. E., Hoessel, J. G., & Oke, J. B. 1986, ApJ, 306, 30
Kelson, D. D., van Dokkum, P. G., Franx, M., Illingworth, G. D., & Fabricant, D. 1997, ApJ, 478, L13
Kinney, A. L., Calzetti, D., Bohlin, R. C., et al. 1996, ApJ, 467, 38
Lubin, L. M., Oke, J. B., & Postman, M. 2002, AJ, 124, 1905
Milvang-Jensen, B. 2003, Ph.D. Thesis, Univ. Nottingham
Poggianti, B. M., Smail, I., Dressler, A., et al. 1999, ApJ, 518, 576
Poirier, S. 2004, Ph.D. Thesis, Louis Pasteur University, Strasbourg I, France
Postman, M., Lubin, L. M., Gunn, J. E., et al. 1996, AJ, 111, 615
Postman, M., Lubin, L. M., & Oke, J. B. 1998, AJ, 116, 560
Postman, M., Lubin, L. M., & Oke, J. B. 2001, AJ, 122, 1125
Schlegel, D. J., Finkbeiner, D. P., & Davis, M. 1998, ApJ, 500, 525
Shectman, S. A. 1985, ApJS, 57, 77
Tran, K. H., Franx, M., Illingworth, G., Kelson, D. D., & van Dokkum, P. 2003, ApJ, 599, 865
Tran, K. H., Kelson, D. D., van Dokkum, P., et al. 1999, ApJ, 522, 39
van Dokkum, P. G. 2001, PASP, 113, 1420
van Dokkum, P. G., Franx, M., Fabricant, D., Illingworth, G. D., & Kelson, D. D. 2000, ApJ, 541, 95
Yee, H. K. C., Ellingson, E., & Carlberg, R. G. 1996, ApJS, 102, 269
Zabludoff, A. I., Franx, M., & Geller, M. J. 1993, ApJ, 419, 47
Zwicky, F., Herzog, E., & Wild, P. 1968, Catalogue of galaxies and of clusters of galaxies (Pasadena: California Institute of Technology (CIT), 1961–1968)